Research Article | Vol. 27, No. 15 | 22 Jul 2019 | OPTICS EXPRESS 21420
Optics EXPRESS

Towards subdiffraction imaging with wire array metamaterial hyperlenses at MIR frequencies

JULIANO G. HAYASHI,[1,2] ALESSIO STEFANI,[1,3] SERGEI ANTIPOV,[4] RICHARD LWIN,[1] STUART D. JACKSON,[5] DARREN D. HUDSON,[4] SIMON FLEMING,[1] ALEXANDER ARGYROS,[1] AND BORIS T. KUHLMEY[1,*]

[1]*Institute of Photonics and Optical Science (IPOS), School of Physics, The University of Sydney, NSW 2006, Australia*
[2]*Optoelectronics Research Centre, University of Southampton, Southampton SO17 1BJ, UK*
[3]*DTU Fotonik, Department of Photonics Engineering, Technical University of Denmark, DK-2800 Kgs. Lyngby, Denmark*
[4]*Department of Physics, Macquarie University, Sydney, New South Wales, Australia*
[5]*Department of Engineering, Macquarie University, Sydney, New South Wales, Australia*
[*]*boris.kuhlmey@sydney.edu.au*

Abstract: We describe the fabrication of metamaterial magnifying hyperlenses with subwavelength wire array structures for operation in the mid-infrared (around 3 μm). The metadevices are composed of approximately 500 tin wires embedded in soda-lime glass, where the metallic wires vary in diameter from 500 nm to 1.2 μm along the tapered structure. The modeling of the hyperlenses indicates that the expected overall losses for the high spatial frequency modes in such metadevices are between 20 dB to 45 dB, depending on the structural parameters selected, being promising candidates for far-field subdiffraction imaging in the mid-infrared. Initial far-field subdiffraction imaging attempts are described, and the problems encountered discussed.

1. Introduction

A combination of conducting/dielectric layers or a subwavelength array of metallic wires embedded in a dielectric exhibit hyperbolic dispersion due to the high anisotropy of the medium [1]. In such hyperbolic metamaterial, high transverse spatial frequencies, which contain subdiffraction information and would be evanescent in conventional isotropic media, can propagate. A curved multilayer metamaterial and a tapered wire array medium, called hyperlenses, can also magnify the guided spatial frequencies, transforming the subdiffraction information into air-propagating waves, allowing subdiffraction imaging in the far-field [2–4].

Far-field subdiffraction imaging with multilayer metal/dielectric metamaterial has been demonstrated at UV [3,5] and visible [6] frequencies. This class of hyperlenses can be fabricated by the deposition of ultra-thin and smooth films, but exhibits high losses and high reflectivity due to its large metal fraction. High transmission can be obtained if the operational region is close to the metal's plasma frequency, where their reflectivity decreases, limiting their operation to narrow bands at UV/visible frequencies if noble metals are employed. Semiconductors can be combined with metal or highly doped semiconductor layers to shift the effective plasma frequency of the metamaterial to lower frequencies, leading to hyperlenses operating at near-infrared (NIR) [7] and at mid-infrared (MIR) [8] frequencies. Recent, theoretical investigations indicate that the losses of multilayer semiconductor material can be reduced by maximizing the mean scattering time of the doped layers and adjusting the layer thickness ratio [9], opening up new possibilities for far-field subdiffraction imaging in the MIR with semiconductor-based metamaterial. However, relatively narrow band, short wavelength operation and lack of a large volume fabrication method are still the main drawbacks of this class of hyperlens.

#367523 https://doi.org/10.1364/OE.27.021420
Journal © 2019 Received 22 May 2019; revised 5 Jul 2019; accepted 6 Jul 2019; published 16 Jul 2019

Optics EXPRESS

Wire array hyperlenses offer very broadband operation, high tunability, potentially lower losses due to the low metal fraction, and alternative low-cost/large-volume fabrication methods like fibre drawing [10–12]. Hyperbolic endoscopes that transport subdiffraction information away from its source have been demonstrated at microwave [13, 14] and at THz frequencies [11], but far-field subdiffraction imaging has not been experimentaly explored yet, to the best of our knowledge. Ankit *et al.* have numerically demonstrated that tapered wire array in a hemispherical sea-urchin geometry can lead to far-field subdiffraction imaging in the NIR [4], but its fabrication still remains a challenge.

Subdiffraction imaging using wire arrays requires a structure containing subwavelength wires separated by a distance smaller than the operational wavelength (λ) [13, 14]. For microwave frequencies, these dimensions are in the mm scale, and wires can be manually assembled in air [13,14]. Alternative fabrication methods, such as the fibre drawing technique, can be employed to attain subwavelength wire array structures operational at shorter wavelengths [10–12]. In fibre drawing, a macroscopic array of metallic wires embedded in a dielectric (wire array preform) is scaled-down by several orders of magnitude, and the neckdown region generates a tapered magnifying hyperlens. Using this approach, Tuniz *et al.* fabricated a wire array metamaterial hyperlens suitable for operation at THz frequencies, containing indium wires embedded in polymer with a wire diameter varying from 10 μm to 80 μm, and wire spacing (Λ) varying from 50 μm to 400 μm. Subdiffraction focusing down to $\lambda/28$ in the THz spectrum and the propagation of subdiffraction information over hundreds of wavelengths was demonstrated [11].

Further size reduction in the metastructure on the small facet of the indium/polymer hyperlens and, consequently, shifting of their operation to wavelengths shorter than the THz, are not feasible with the drawing approach due to the rheological properties of the selected materials (indium and polymer). The Plateau-Rayleigh instability [15], which is the tendency of a liquid column to break into droplets, limits the wire diameter and wire spacing to a few microns in the indium/polymer system [16, 17], restricting the operation wavelength of the metamaterial to the far-infrared. Recently, we have demonstrated that such wire size limitation can be overcome by replacing the materials with tin and soda-lime glass and optimizing the drawing/stretching process [12]. Uniform wire array metamaterial fibres with wire diameter and spacing in the few hundreds of nm scale were obtained, resulting in wire array metamaterial that could operate at wavelengths as short as the mid-infrared.

Besides the fabrication challenges related to the size and uniformity of submicron wires, their typically high optical losses at MIR frequencies represent an enormous constraint in the development of MIR hyperlenses. The quasi-TEM modes that could lead to subdiffraction images exhibit losses in the dB/μm scale [18], which limits the overall length of the hyperlens to the few hundred-micron scale (depending on its structural parameters and materials selected) which is not trivial to achieve.

In the present work, we propose a wire array tapered hyperlens structure that could lead to far-field subdiffraction imaging in the MIR and analyze its optical loss as a function of overall length for two different material combinations (tin/soda-lime and gold/silica). Such numerical modeling indicates the typical length and structural transition required to limit the hyperlenses' overall losses to 50 dB when operating in the MIR. Then, we demonstrate the fabrication of wire array hyperlenses in the 100 μm length scale with an expected overall loss lower than 50 dB. The structures contain wires with an averaged diameter (d_{avg}) and an averaged wire spacing (Λ_{avg}) as small as a few hundred nm in its smallest facet, and, consequently, the operation wavelength becomes as short as λ= 3 μm. Finally, we describe far-field subdiffraction imaging attempts with the fabricated hyperlenses, and discuss in detail the problems encountered and possible solutions.

Optics EXPRESS

2. Overall loss estimation of wire array hyperlenses in the MIR

In subwavelength wire array media, the hyperbolic dispersion allows the propagation of modes with high transverse spatial frequencies, called quasi-TEM modes [19], which carry subdiffraction information and can lead to super-resolution imaging [2, 11, 13, 14]. The losses of the quasi-TEM modes are strongly dependent on the material components, wire diameter (d), lattice spacing (Λ), the wavelength of operation (λ), and their transverse wavevector component ($k_\perp$) [18]. When a hyperlens is considered (*i.e.* a tapered wire array structure), the overall length and profile of the tapered transition also have a strong influence on the resultant loss of the metadevice.

When applications of wire array metamaterial fibres in the MIR are concerned, tin wires embedded in soda-lime glass are an interesting system from a fabrication perspective (low cost, drawable and with high chemical compatibility) [18], albeit with poor optical performance. Numerical simulations indicate that several metals are expected to exhibit lower losses than tin in an equivalent structure (gold, aluminium, silver), but these material combinations are considerably more challenging to fabricate with the drawing technique [18]. Of those options, only gold wires embedded in silica glass have been successfully co-drawn, with the drawback of high cost and challenge in the fabrication of uniform drawn sub-micron wires with no gaps [20]. Here, we study the optical losses in hyperlenses made of the two systems (tin/soda-lime and gold/silica), which represent a feasible/low-cost fabrication option and an option with better optical performance, respectively.

Figure 1 shows the simulated losses in dB/μm for the quasi-TEM mode in an indefinite hexagonal wire array structure made of tin wires embedded in soda-lime glass (Fig. 1(a)) and gold wires embedded in silica (Fig. 1(b)) for $\lambda = 3\ \mu$m. The effective refractive indices (n_{eff}) of the modes were obtained with finite element software (COMSOL) [18], and their respective optical losses were calculated using

$$\alpha = \frac{40\pi\kappa}{\lambda \ln 10}, \tag{1}$$

where κ is the imaginary part of n_{eff}, and λ is the wavelength of light in microns. In both cases, the structure has a fixed $d/\Lambda = 0.5$ and three different transverse spatial frequency components are considered ($k_\perp = 0$, $k_\perp = 0.5k_{\perp\max}$ and $k_{\perp\max}$). The $k_{\perp\max}$ corresponds to the transverse wave vector component matching one of the edges of the first Brillouin zone of the hexagonally arranged wire array ($k_{\perp\max} = (\pi/\Lambda)(2/\sqrt{3})$), which will result in a resolution close to the maximum of the hyperlens if they are detected in an imaging experiment [21] (p. 116).

According to Fig. 1, the losses of the high-$k_\perp$ quasi-TEM modes in subwavelength wire array structures can vary from 0.1 to 1 dB/μm ($\lambda = 3\ \mu$m) depending on the wire diameter/spacing and the materials selected. The losses increase for smaller wires, in agreement with the behavior seen in [18]. Because of these characteristic high losses, a steep and short transition between the two facets of the hyperlens and/or a steeper transition on the small facet side are required to minimize the overall losses of the propagating high-$k_\perp$ modes such that they remain detectable.

A schematic of our proposed hyperlens for subdiffraction imaging in the MIR is seen in Fig. 2(a). The taper has wire diameters linearly varying from 400 nm to 800 nm from the small to the large facets, respectively, a magnification factor of 2× and a fixed $d/\Lambda = 0.5$. The overall optical loss of this hyperlens can be estimated by discretizing the tapering transition into several small slices along its length and multiplying it with the loss of the respective cross-sectional structure (Fig. 1). The error of this approximation decreases with decreasing slice length but assumes the transition is adiabatic. Here, we consider the nominal overall loss of the hyperlens as the loss of the quasi-TEM modes with $k_{\perp\max}$, because they have the highest losses among the high-$k_\perp$ modes and will lead to the highest resolution.

Optics EXPRESS

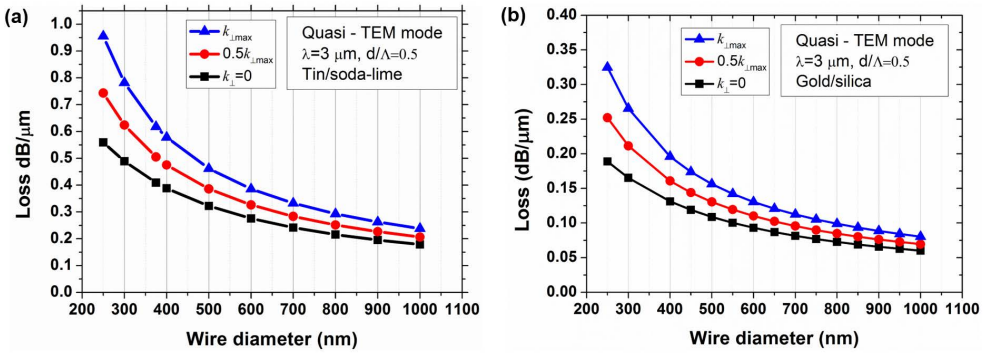

Fig. 1. Optical loss in dB/μm for the indefinite hexagonal wire array structure with $d/\Lambda = 0.5$, as a function of the wire diameter, at $\lambda = 3\ \mu$m. The black, red and blue curves represent the modes with transverse wave vector equal to 0, $0.5k_{\perp\max}$, and $k_{\perp\max}$ respectively, where $k_{\perp\max} = (\pi/\Lambda)(2/\sqrt{3})$ for a hexagonally arranged array. (a) Tin wire array embedded in soda-lime glass. (b) Gold wire array embedded in silica.

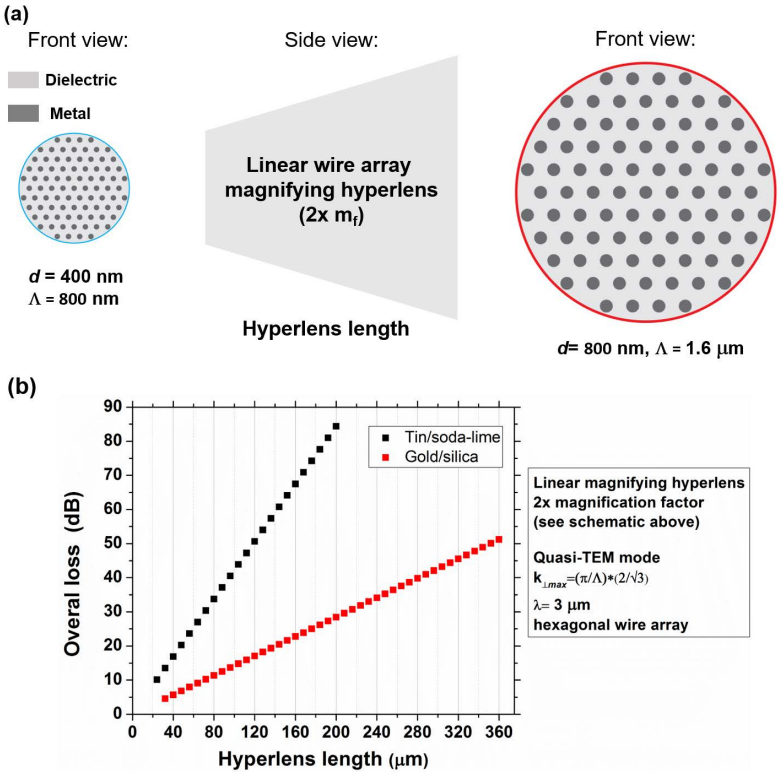

Fig. 2. (a) Schematic of the proposed linear wire array magnifying hyperlens with 2× magnification and d varying from 400 nm to 800 nm, $d/\Lambda = 0.5$, hexagonally arranged. (b) Overall loss in dB for the quasi-TEM mode ($k_{\perp\max}$) for hyperlens illustrated in (a) with tin/soda-lime and gold/silica system, calculated with the losses of the respective indefinite wire arrays presented in Fig. 1.

Optics EXPRESS

Figure 2(b) shows the expected overall loss of the proposed hyperlens (Fig. 2(a)) as a function of the overall length for the systems selected (tin/soda-lime - black dots, and gold/silica - red dots). Considering the limiting overall loss as 50 dB for a feasible imaging attempt, the proposed metadevice must have an overall length smaller than 120 μm for the tin/soda-lime system, or smaller than 360 μm for the gold/silica system. The fabrication of uniform wire array tapered samples in this scale of length, and wire diameter is challenging and will be described in the next section.

Note that these estimated values of the maximum overall lengths are strongly related to the structural parameters selected for the magnifying hyperlens and how they vary over length. Therefore, they should be considered as mere indications of the transitions required. It is well known from the tapering of optical fibres [22, 23] that an adiabatic transition is preferable to minimize the optical loss in a tapered waveguide, which is probably not the case for the shortest linear transition analysed in Fig. 2(b). In such adiabatic transitions, the angle of the taper must be small enough that there is negligible power coupling between the modes. Thus, a strict loss evaluation must take into account such modal coupling, which would be computationally very challenging for this heavily multiscale problem. Our method discussed above (and the losses of Fig. 2(b)) must be considered an approximation, employed merely to provide an estimation and a qualitative comparison between the different systems.

3. Hyperlens fabrication

A wire array hyperlens can be obtained from a stretching process of a macroscopic version of a wire array structure, *i.e.*, a metamaterial preform or a metamaterial fibre. Such a method can be conventional fibre drawing [10, 11] or fibre tapering, similar to the tapering of traditional optical fibres [22, 23]. Here, we developed a vertical stretching setup to fabricate tapered wire array structures from metamaterial preforms/fibres. Steep transitions with an overall length in the few hundreds of micron scale are demonstrated, which is a requirement of MIR hyperlenses due to their typical optical losses (Fig. 2(b)).

A schematic of the stretching setup and tapering fabrication is seen Fig. 3(a). The heating element consists of a platinum/iridium alloy sheet of 50 μm thickness with a center hole of 1.2 mm in diameter (inset of Fig. 3(a)). A conventional pipette puller P-97 from Sutter Instruments is used as power supply/controller [24] to heat the alloy element with an AC electrical current on a 10 s time scale. The preform is held by two drill chucks and aligned with the hole in the alloy filament with three micrometric stages coupled to the top drill chuck. When the electric current heats the alloy element, the viscosity of the glass locally decreases, and the sample is stretched by gravity. The pulling tension is predetermined by the weight attached to the bottom of the preform (Fig. 3(b)). A picture of the stretching setup is seen in Fig. 3(c).

The standard metamaterial fibre employed here in the hyperlens fabrication contains approximately 500 wires, has an outside diameter (OD) of 400 μm, average wire diameter (d_{avg}) of 4 μm and averaged wire spacing (Λ_{avg}) of 8 μm (Fig. 3(d)). The details regarding its fabrication and the suppression of the Plateau-Rayleigh instabilities are fully described in [12, 21]. An example of a typical steep tapering transition region fabricated from this standard metamaterial fibre using the stretching setup is seen in Fig. 3(e). The vertical arrows represent the region that could be selected to achieve a 3× magnifying hyperlens with a wire structure varying from approximately $d_{\text{avg}} = 300$ nm and $\Lambda_{\text{avg}} = 600$ nm (OD = 30 μm) to $d_{\text{avg}} = 900$ nm and $\Lambda_{\text{avg}} = 1.8\,\mu$m (OD = 90 μm), over an approximately 100 μm length.

The fabrication of such steep tapering transitions results from the minimization of the hot-zone length and maximization of the pulling tension employed (around 49 N/mm^2 before stretching). The hot-zone length, which is the region where the sample's temperature is high enough to be stretched, is proportional to the thickness of the filament, but also depends on several factors such as: the ratio between the size of the preform and that of the hole in the filament, the current

Optics EXPRESS

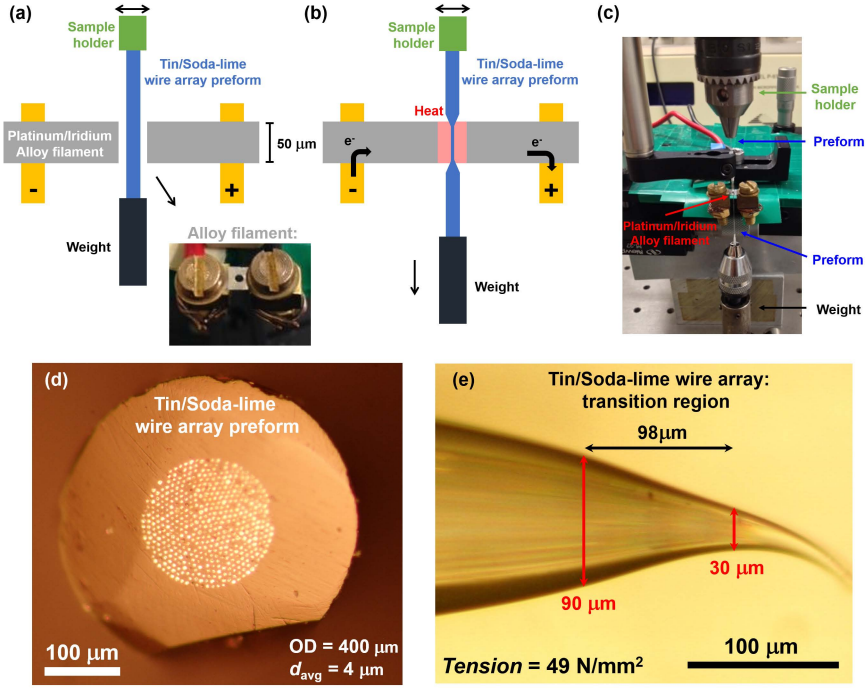

Fig. 3. (a) Schematic of our stretching setup developed to fabricate steep and short wire array tapered transitions. (b) Schematic of the stretching process, where a metamaterial preform is locally heated by a platinum/iridium alloy filament (50 μm thickness) and a bottom weight stretches the sample by gravity. (c) Picture of the stretching setup, composed by a sample holder (drill chucks) employed to hold and align the preform, the alloy filament (hot-zone) and the pulling weight. (d) Micrograph of the standard tin/soda-lime wire array metamaterial preform employed through this work. The outside diameter of 400 μm (d_{avg} = 4 μm and Λ_{avg} = 8 μm), containing approximately 500 wires. (e) Example of a typical transition region fabricated with an initial tension by area of 49 N/mm^2. The red arrows indicate a 3× magnification hyperlens with a length of 98 μm.

employed in the heating element, the time of the heating process, and the heat dissipation of the system. Though it is hard to measure or simulate its length, the transitions achieved in such a system indicates a hot-zone region in the mm scale.

In early experiments using a different setup and lower tension, microscope images suggested the liquid tin receded from holes in the smallest part of the taper. With the high tension and fast heating of the final setup, we could not find any evidence of the metal receding. Both optical and electron microscope images suggest metal wires extend continuously all the way through the taper. However microscope images alone are insufficient to ascertain the continuous nature of the wires, and this will require further analysis.

The transition region with the desired range of structural parameters is extracted from the tapered wire array metamaterial fibre in an embedding process with a thin metallic foil, giving rise to the hyperlens. This selection depends on the targetted magnification factor (ratio between the outside diameters of both ends of the transition), resolution and total optical loss intended for the final metadevice. Figure 4(a) shows a schematic of the desired transition for a 3× magnifying hyperlens and where the metallic foil should be fixed (black dotted line). In such a process, the alignment between the sample and the foil is crucial and not trivial.

Optics EXPRESS

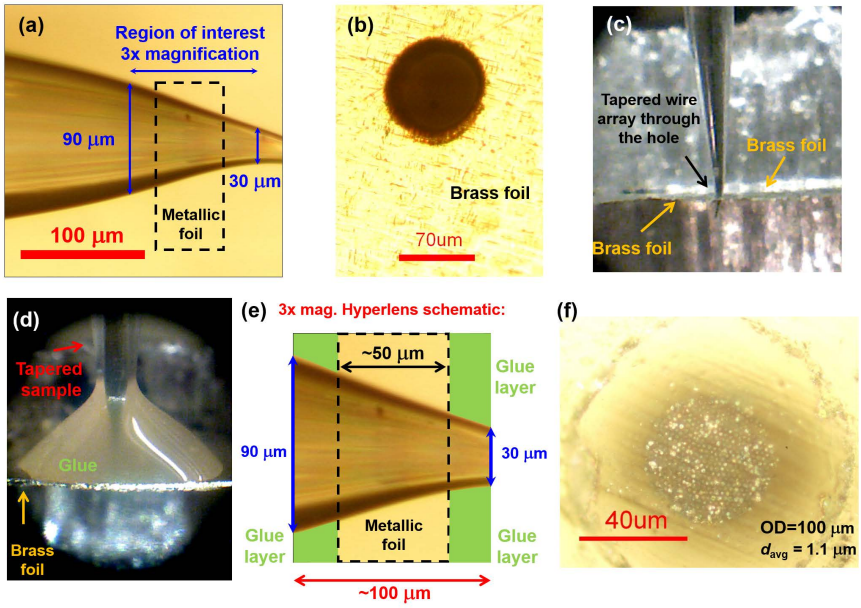

Fig. 4. (a) Example of a tapered metamaterial sample and the region of interest for a 3× magnifying hyperlens, with the desired position of the metallic foil (black dotted rectangle) for the embedding process. (b) Picture of a 70 μm hole fabricated by a high power femtosecond laser (Macquarie University, ANFF OptoFab node, Sydney, Australia), in a brass foil with 50 μm thickness. (c) Alignment of the tapered sample through the hole micro-machined in brass foil. (d) Gluing of the sample with an epoxy adhesive (yellow region). (e) Schematic of a 3× magnifying hyperlens after the extraction process is concluded. (f) Example of the large facet of a hyperlens with OD = 100 μm and $d_{\text{avg}} = 1.1$ μm.

In our developed embedding process, a precise hole is drilled in a thin metallic foil with a high power femtosecond laser. Figure 4(b) shows a 70 μm hole fabricated in a brass foil with a thickness of 50 μm. With micrometer stages and a microscope, the tapered sample is introduced through the laser drilled hole of the metallic foil. Figure 4(c) shows a picture of this alignment process, where it is possible to visualize the brass foil and a small part of the hyperlens below it. Because the diameter of the laser-drilled hole is slightly smaller than the outside diameter of the large facet of the desired hyperlens, the sample stops at the intended position (Fig. 4(a)).

A tiny portion of epoxy glue is manually deposited on both sides of the foil, as seen in Fig. 4(d), the large side of the sample is cleaved, and both facets of the transition are polished. The side containing the large facet of the hyperlens is polished over several separated cycles using polishing papers with decreasing grit size. For the small and more fragile facet of the hyperlens, a polishing cycle with the finest grit and low pressure is enough to achieve the desired result. Careful and slow polishing, combined with a regular visualization and measurement of the resulting structure with a microscope, allows the desired transition to be selected. Figure 4(e) shows a schematic of a 3× magnified hyperlens after the extraction process is concluded, and Fig. 4(f) shows the large facet of a hyperlens after the polishing (OD = 100 μm, $d_{\text{avg}} = 1$ μm).

The embedding process described above is quite flexible because different regions of a tapered sample can be selected by adjusting the size of the laser-drilled hole. Thinner metallic foils with a thickness of 13 μm (Starrett 667-1/2 feeler gauge) and 5 μm (Goodfellow, CU020200) can be used to embed shorter transition regions.

Optics EXPRESS

4. Far-field imaging attempt with wire array hyperlenses in the MIR

The diffraction limit of an optical system in the far-field arises from the nature of the light scattering and the spatial bandwidth of free-space. When an incident beam of light scatters off an object into an isotropic medium with refractive index n, the object's information is transferred to a wide spectrum of wavevector components, which can be propagating waves ($|k_\perp| < n|k_0| = 2\pi n/\lambda_0$, considering $\perp$ the plane transverse to the propagation direction z) or evanescent waves ($|k_\perp| > n|k_0|$ with imaginary k_z). Because the evanescent waves possess larger transverse wavevector components, they carry finer details about the object than the scattered propagating waves. In a conventional optical system, such evanescent high $k_\perp$ waves decay exponentially, being effectively attenuated before reaching the image plane. Consequently, part of the information about the object is lost, and the resolution of the detected image is always "diffraction limited".

In magnifying hyperlenses, the hyperbolic dispersion allows the propagation of the high spatial frequencies and, because the structural parameters of the metamaterial vary along the length, the high spatial frequencies are transformed into lower spatial frequencies [2,14]. If the magnification factor is high enough to transform the high spatial frequencies to frequencies smaller than k_0, they become waves able to propagate in free space after the metamaterial, and subdiffraction far-field imaging is obtained [2].

The diffraction limit of an imaging system can be probed with the far-field image of a double-circular aperture with varying center-to-center spacing. If their center-to-center separation is larger than the system's diffraction limit, both circular apertures are well defined in the image plane, *i.e.*, an intensity profile along the apertures and parallel to their separation exhibits two distinct peaks. If their center-to-center separation is smaller than the diffraction limit, the image of a double-circular aperture results in a single intensity maximum and only one peak is defined in an intensity profile. Thus, far-field subdiffraction imaging with a magnifying hyperlens could be demonstrated if the image of an unresolved double-circular aperture (single intensity maximum) becomes resolved with the insertion of the hyperlens in the optical system. In the next subsections, two different imaging experiments using different types of apertures are described aiming to demonstrate far-field subdiffraction imaging with our hyperlenses.

4.1. Imaging of apertures FIB-milled on a gold film/borosilicate slide

The first experimental setup for far-field imaging with our hyperlenses in the MIR is illustrated in Fig. 5(a). The collimated output beam from an Er^{3+} doped ZBLAN fibre laser (Fig. 5(b), elliptically-polarized CW output power up to 2 W [21], is focused with a ZnSe aspheric lens (NA = 0.67 and f= 12.7 mm) onto the aperture to be imaged, which is positioned in the lens's focal point. Figure 5(c) shows a double-aperture milled with a FIB in a 100 nm gold film deposited on a borosilicate slide and its alignment with the wire array region of the hyperlens. A second GeSbSe aspheric lens (NA = 0.56, f = 4 mm) is employed to collect the light diffracted through the aperture and to reconstruct its image in the image plane, where an infrared beam-profile camera is aligned. For our experiments, a Spiricon/Pyrocam IV solid-state/pyroelectric camera (OPHIR Photonics) was used containing an array of 320x320 pixels, a pixel size of 80 μm, and a nominal noise limit around 64 nW/pixel [25].

Several hyperlenses where fabricated with slightly different magnification factors (from 1.4× to 2.2×), structural parameters ($d/\Lambda = 0.5$, d_{avg} varying from 500 nm to 1.4 μm), overall length on the 100 μm scale and expected overall loss between 20 dB to 45 dB). Before any subdiffraction far-field imaging was attempted with the hyperlenses, *i.e.*, the resolving of a double-circular aperture with spacing smaller than the system's diffraction limit, the fabricated samples were tested on the imaging of larger double-circular apertures that transmit more light and are easier to align and detect.

Optics EXPRESS

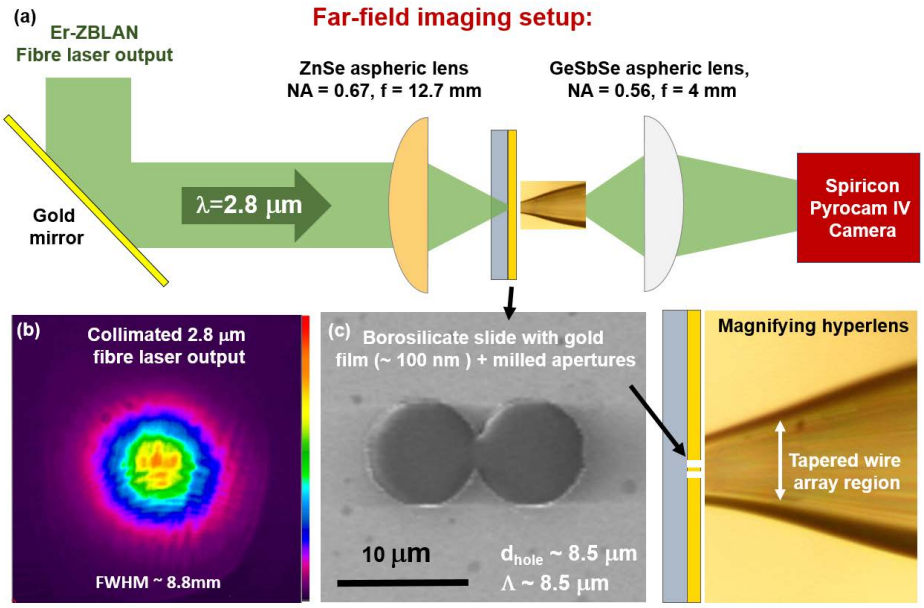

Fig. 5. Schematic of the first far-field imaging setup: (a) Er-ZBLAN fibre laser with output wavelength centered at 2.8 μm ((b) Intensity profile of the collimated beam), ZnSe aspheric lens to focus the light through the apertures, hyperlens, GeSbSe aspheric out-coupling lens to image the transmitted light in the far-field, GeSbSe aspheric out-coupling lens to image the transmitted light in the far-field, and beam-profile solid-state/pyroelectric camera Spiricon aligned in the image plane. (c) A double-aperture milled with FIB in a borosilicate slide covered with a 100 nm gold film, and its alignment with the wire array region of the hyperlens. The circular apertures have diameter and spacing around 8.5 μm.

Figure 6(a) shows the far-field image of the 8.5 μm double-aperture (Fig. 5(c)) using the experimental setup described in Fig. 5(a), in-coupling ZnSe aspheric lens (NA = 0.67, f= 12.7 mm), out-coupling GeSbSe aspheric lens (NA = 0.56, f = 4 mm), with no hyperlens in the optical setup, and the Spiricon camera 28 cm away from the out-coupling lens. The NA of the in-coupling lens is selected to achieve a focused spot size slightly larger than the aperture to maximize the transmitted power. Similarly, the NA of the out-coupling lens is selected according to the desired diffraction limit of the system and the desired magnification factor of the image in the image plane. Such magnification depends on the focal length and the distance of the out-coupling lens from the image plane (thin lens equation). The estimated magnification factor is 69× for the setup described in Fig. 5(a), which is in good agreement with the magnification of the double-aperture observed in Fig. 6(a). In this configuration, with a wavelength of 2.8 μm, the diffraction limit of the system considering an incoherent illumination is expected to be around 2.5 μm (Abbe's diffraction limit = λ/(2NA) [26, 27], where NA is the numerical aperture of the out-coupling lens). As expected, the intensity profile on the horizontal axis of the image (dotted lines) shows that the two circular apertures are well defined, once their distance center-to-center (8.5 μm) is larger than the optical system's expected diffraction limit.

After the far-field image of the double-circular aperture was obtained, every fabricated hyperlens was aligned face-to-face with the aperture using a micrometric stage and a portable microscope (Fig. 5(c)). The focus of the out-coupling lens was slightly re-aligned to focus the image again in the image plane. The typical resultant image is seen in Fig. 6(b), where no light is

Optics EXPRESS

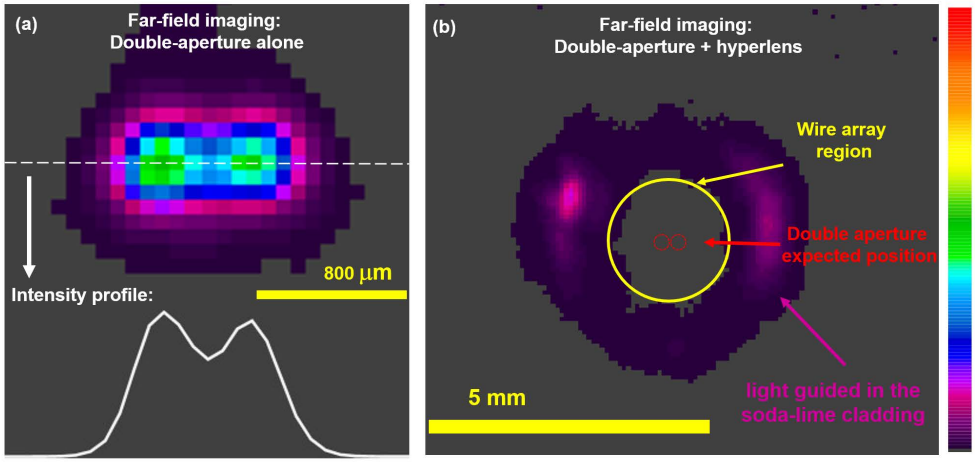

Fig. 6. (a) Far-field image of the double aperture alone, performed with an in-coupling asphreric ZnSe lens with NA = 0.67 (f= 12.7 mm), an out-coupling GeSbSn aspheric lens with NA = 0.56 (f= 4 mm), $\lambda = 2.8$ μm, and the Spiricon camera 28 cm away from the out-coupling lens. (b) Typical far-field image obtained coupling a magnifying hyperlens after the double aperture, where it is possible to visualize some light guiding in the soda-lime cladding of the hyperlens (purple region) and no light in the wire array region (yellow circle). Scale bars refer to the scale on the camera detector.

detected from the wire array region (the region marked in yellow) and no double-circular aperture is seen (expected position indicated in red), probably due to the high loss of the hyperlens. The light guided in the soda-lime cladding of the hyperlens (purple region) may be a result of a bad input coupling into the glass (small gap between the aperture and the hyperlens), leakage from the wire region due to imperfections (wire diameter fluctuation along length or discontinuity in the wires) or could correspond to ordinary waves (electric field transverse to the anisotropy axis, which do not “see" the wires and hence diffract) [28]. The power density by pixel in the image plane could be improved by increasing the input power, improving the coupling between the aperture and the hyperlens, and/or using a hyperlens with a lower overall loss (shorter sample with lower magnification factor).

Imaging attempts with increasing the input power incident in the apertures from a few hundreds of mW to 1 W were performed, but the samples were damaged due to the melting of the tin wires, which occurs at 232 ° C. Figure 7 shows the cross-section micrograph of the small facet of a magnifying hyperlens before (Fig. 7(a)) and after (Fig. 7(b)) an imaging attempt with an input power of 800 mW ($\lambda = 2.8$ μm) incident in the 8.5 μm double-aperture (Fig. 5(c)). The solidified shiny circular drops seen in Fig. 7(b) indicate that the metal melted and came out of the hyperlens' surface. Consequently, increasing the power above a few hundred milliwatts is not a viable alternative to obtain a detectable signal in the wire array region for the typical tin/soda-lime hyperlens fabricated.

Optics EXPRESS

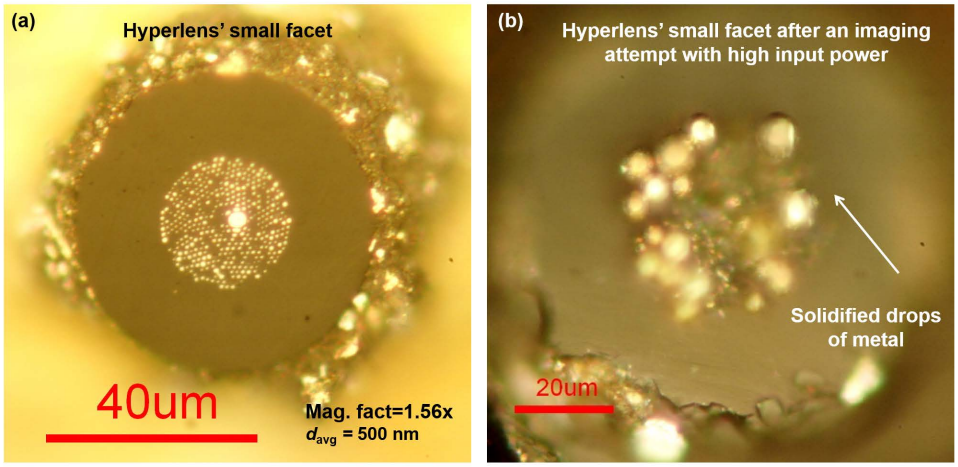

Fig. 7. Cross-section micrograph of the small facet of a tin/soda-lime magnifying hyperlens (wire diameter varying from approximately 500 nm to 780 nm, $d/\Lambda = 0.5$, length of 80 μm, expected overall loss of 30 dB, and magnification factor 1.56×) before (a) and after (b) an imaging attempt using high CW input power up to 800 mW ($\lambda = 2.8$ μm). The solidified shiny drops in (b) indicate that the metal melted and came out of the hyperlens' surface.

4.2. *Imaging of apertures FIB-milled on the hyperlens' small facet*

A second imaging experiment approach was attempted to eliminate the uncertainty in the coupling between the apertures and the wire array region. In this second configuration, the apertures milled on the borosilicate slide were replaced by apertures directly FIB-milled on the small facet of a low-loss hyperlens previously covered with a 200 nm gold film (Fig. 8(a)). Figure 8(b) shows a micrograph of three milled apertures and their respective diameters (4.5 μm, 2.6 μm and 1.7 μm), where it is possible to visualize their alignment with the wire array region. The overall length of this hyperlens was minimized to decrease its expected overall loss to 20 dB, which was achieved by embedding the sample in a 13 μm stainless steel foil and polishing both sides until an overall length around 40 μm was obtained. The averaged size of the wires in this sample varies from 500 nm to 650 nm along the small to the large facet ($d/\Lambda = 0.5$), resulting in a magnification factor of 1.3×.

Magnified far-field images of the 4.5 μm (Fig. 8(c)) and 2.6 μm (Fig. 8(d)) apertures were individually obtained using the experimental setup described in Fig. 5(a) (without the borosilicate slide) and aligning the focused beam separately through each aperture to maximize the transmitted power. Magnified far-field image of the 1.7 μm aperture was not obtained due to its high in-coupling loss. Clearly, for the 4.5 μm and 2.6 μm apertures, the losses are low enough for signal to be transmitted, and the propagation in the wire array appears diffractionless. Note that their images in the imaging plane are magnified due to the magnification factor of the hyperlens and the out-coupling lens. However, the image of a single aperture cannot be used to determine the magnification or resolution limit, as it could be indistinguishable from the point spread function. Unfortunately, far-field imaging of the three milled apertures (or any pair) in a single image with the same setup, as would be required to evaluate the magnification and the diffraction limit of the system, was not obtained because the power density of the image in this configuration was smaller than the noise limit of our camera. This simultaneous imaging requires a larger spot size incident on the apertures (large enough to equally illuminate the three or any pair of them), which decreases considerably the light coupled through the apertures into the hyperlens and increases

Optics EXPRESS

the overall loss of the optical system. Increasing the input power to compensate such coupling loss is not a viable option because any misalignment of the beam can locally melt the wires or damage the gold film.

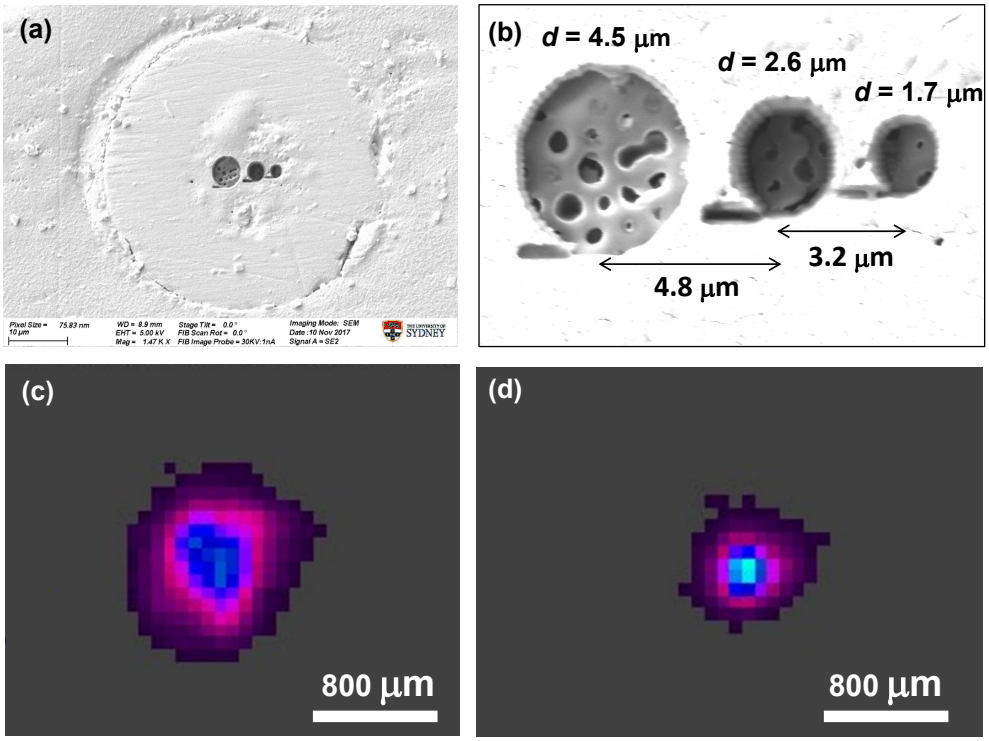

Fig. 8. (a) Micrograph of the hyperlens' smaller facet covered with a sputtered gold film and three circular apertures FIB milled on the wire array region (light input). (b) Zoom image of the apertures and their respective diameters: 4.5 μm, 2.6 μm and 1.7 μm. Far-field images of the 4.5 μm aperture (c) and 2.6 μm aperture (d), using an in-coupling ZnSe aspheric lens (NA = 0.67 and f= 12.7 mm), an out-coupling GeSbSe aspheric lens (NA = 0.56, f = 4 mm) to collect the light out-coupled from the large facet of the hyperlens, and the array camera aligned 6 cm away from the metadevice. In (c) and (d) scale bars refer to the scale on the camera detector.

According to our numerical simulations, the expected transmission loss of the quasi-TEM mode with $k_{\perp \max}$ at $\lambda = 3\mu$m in the hyperlens employed in Figs. 8(c)-8(d) is around 20 dB. The experimental overall losses calculated measuring the input power before the apertures and after the hyperlens was 29 dB and 33 dB for the imaging of Figs. 8(c) and 8(d), respectively. This difference could be explained by a high coupling loss between the focused beam and the milled aperture (incident spot size too large), Fresnel reflections at the hyperlens interfaces, and leakage from the wire array region to the hyperlens' soda-lime cladding that is not detected by the camera due to defects or the initial coupling of diffracting ordinary waves (TE modes). Further study is required to understand this discrepancy fully and to filter the ordinary waves that leak from the wire array structure and usually have lower losses, adding considerably to the expected noise level [29].

Further improvement in the detection using a more sensitive array camera could help in the far-field imaging of large apertures using low magnification hyperlenses, like those employed here.

Optics EXPRESS

Alternatively, preliminary modeling indicates that shifting the wavelength of operation to slightly larger wavelengths could decrease the optical loss of our metadevices (for example, losses ~1.4× smaller in dB at 5 μm wavelength, in comparison to 3 μm wavelength presented here). However, demonstrating far-field subdiffraction imaging of subwavelength apertures seems unfeasible with such tin/soda-lime hyperlenses (even at 5 μm wavelength): to achieve real sub-diffraction imaging, a magnification larger than 1.5 is required (since a factor 1.5 could be simply achieved through an immersion lens with the same refractive index as the glass background), and the object to be imaged will require accordingly smaller apertures. The smaller overlap of the input beam with the apertures, the drastic power loss through sub-wavelength apertures, and the increased losses due to the inevitable longer length of higher magnification tapers all combine to make the tin/soda-lime system unlikely to be successful. Steeper tapering transitions with overall length in the few tens of microns could bring the overall loss of the metadevices to a level allowing detection, but their fabrication is remarkably challenging. Thus, a considerable improvement in the hyperlens' optical performance is essential, which could be achieved changing the tin wires for gold wires, as indicated by our modeling shown in Fig. 2.

5. Conclusion

We have numerically investigated the optical losses of wire array metamaterials to understand the typical tapering transitions (wire diameter, wire spacing and overall length) required to achieve hyperlenses with losses in the MIR that could permit successful imaging experiments (wavelength operation around 3μm). The losses of the high spatial frequency quasi-TEM modes, *i.e.*, the modes that carry subwavelength information and lead to far-field subdiffraction imaging, can vary from 0.1 dB/μm to 1 dB/μm depending on the structural parameters or the materials selected (tin or gold wires). Thus, considering the limiting overall loss for an imaging experiment as 50 dB, our modeling indicates that tin/gold hyperlenses with subwavelength wires must have an overall length in the few hundred-micron scale.

The fabrication of short/steep tapered wire array samples and the embedding process to extract the hyperlens were demonstrated, with samples containing averaged wire diameter varying from 500 nm to 1.2 μm along the taper's length. Magnifying hyperlenses with overall length in the 100 μm scale were obtained, with an expected overall loss of the quasi-TEM modes between 20 dB to 45 dB, depending on the structures selected.

Far-field imaging attempts with our tin/soda-lime hyperlenses have shown that the coupling between the aperture and the hyperlens, as well as the high losses of the metamaterial are the main problems in this challenging experiment. We eliminated the input coupling uncertainty by milling the apertures directly on the small facet of the hyperlenses after covering it with a gold film. Far-field images of the apertures were obtained individually when focusing the input beam into every aperture separately, demonstrating diffractionless propagation of light. Unfortunately, the simultaneous far-field imaging of any pair of the apertures was not obtained because it requires a larger incident spot size, which decreases considerably the amount of light coupled through the apertures into the hyperlens. Increasing the input power to compensate such coupling loss and metamaterial loss is not a viable option because any misalignment of the beam can locally melt the wires or damage the gold film.

In conclusion, further improvement in the detection and/or reduction of the hyperlens losses could lead to far-field imaging of large apertures for an operational wavelength around 3 μm. However, far-field subdiffraction imaging of subwavelength apertures in this regime does not seem feasible with our tin/soda-lime hyperlenses, once smaller apertures and large magnification factors are necessary. A considerable increase in the hyperlens' optical performance is required, which could be achieved by changing the tin wires for gold wires, as indicated by our modeling shown in Fig. 2. Preliminary simulations and fabrication attempts indicate that other material combinations and fabrication approaches could also increase the hyperlens' optical performance

in the future, such as the drawing of metamaterial fibers containing AgCu wires embedded in borosilicate glass or the coating of tapered hole array samples with aluminium by chemical vapor deposition.

Funding

Science without Borders Program (CAPES, grant 9468/13-7); Newton International Fellowship (NF170629); European Union Horizon 2020 research and innovation programme (Marie Sklodowska-Curie grant agreement No 708860); Australian Research Council (Discovery Project scheme number DP120103942 and DP140104116).

Acknowledgments

Juliano Hayashi thanks the Science without Borders Program (CAPES) and the Royal Society for their funding through the grant 9468/13-7 and the Newton International Fellowship (NF170629), respectively. The authors would like to thank Benjamin Johnson and Alex Stokes for the laser drilling of the brass foils employed in the hyperlenses' embedding process (Macquarie University, ANFF OptoFab node, Sydney, Australia). The authors acknowledge the facilities and the scientific and technical assistance of Microscopy Australia at the Australian Centre for Microscopy & Microanalysis at the University of Sydney.

This project was performed in part at the Optofab node of the Australian National Fabrication Facility (ANFF) using Commonwealth and NSW State Government funding.

References

1. A. Poddubny, I. Iorsh, P. Belov, and Y. Kivshar, "Hyperbolic metamaterials," Nat. Photonics **7**, 948–957 (2013).
2. Z. Jacob, L. V. Alekseyev, and E. Narimanov, "Optical hyperlens: far-field imaging beyond the diffraction limit," Opt. Express **14**, 8247–8256 (2006).
3. Z. Liu, H. Lee, Y. Xiong, C. Sun, and X. Zhang, "Far-field optical hyperlens magnifying sub-diffraction-limited objects," Science **315**, 1686 (2007).
4. A. Bisht, W. He, X. Wang, L. Y. L. Wu, X. Chen, and S. Li, "Hyperlensing at NIR frequencies using a hemispherical metallic nanowire lens in a sea-urchin geometry," Nanoscale **8**, 10669–10676 (2016).
5. H. Lee, Z. Liu, Y. Xiong, C. Sun, and X. Zhang, "Development of optical hyperlens for imaging below the diffraction limit," Opt. Express **15**, 15886–15891 (2007).
6. J. Rho, Z. Ye, Y. Xiong, X. Yin, Z. Liu, H. Choi, G. Bartal, and X. Zhang, "Spherical hyperlens for two-dimensional sub-diffractional imaging at visible frequencies," Nat. Commun. **1**, 143 (2010).
7. S. Schwaiger, A. Rottler, M. Bröll, J. Ehlermann, A. Stemmann, D. Stickler, C. Heyn, D. Heitmann, and S. Mendach, "Broadband operation of rolled-up hyperlenses," Phys. Rev. B **85**, 235309 (2012).
8. M. Desouky, A. M. Mahmoud, and M. A. Swillam, "Tunable mid IR focusing in InAs based semiconductor hyperbolic metamaterial," Sci. Rep. **7**, 15312 (2017).
9. W. S. Hart, A. O. Bak, and C. C. Phillips, "Ultra low-loss super-resolution with extremely anisotropic semiconductor metamaterials," AIP Adv. **8**, 025203 (2018).
10. A. Tuniz, B. Kuhlmey, R. Lwin, A. Wang, J. Anthony, R. Leonhardt, and S. Fleming, "Drawn metamaterials with plasmonic response at terahertz frequencies," Appl. Phys. Lett. **96**, 191101 (2010).
11. A. Tuniz, K. J. Kaltenecker, B. M. Fischer, M. Walther, S. C. Fleming, A. Argyros, and B. T. Kuhlmey, "Metamaterial fibres for subdiffraction imaging and focusing at terahertz frequencies over optically long distances," Nat. Commun. **4**, 2706 (2013).
12. J. G. Hayashi, R. Lwin, A. Stefani, S. Fleming, B. T. Kuhlmey, and A. Argyros, "Fabrication of soft-glass based wire array metamaterial fibers for applications at infrared frequencies," J. Light. Technol. (to be published).
13. P. A. Belov, Y. Zhao, S. Tse, P. Ikonen, M. G. Silveirinha, C. R. Simovski, S. Tretyakov, Y. Hao, and C. Parini, "Transmission of images with subwavelength resolution to distances of several wavelengths in the microwave range," Phys. Rev. B **77**, 193108 (2008).
14. P. A. Belov, G. K. Palikaras, Y. Zhao, A. Rahman, C. R. Simovski, Y. Hao, and C. Parini, "Experimental demonstration of multiwire endoscopes capable of manipulating near-fields with subwavelength resolution," Appl. Phys. Lett. **97**, 191905 (2010).
15. S. Tomotika, "On the instability of a cylindrical thread of a viscous liquid surrounded by another viscous fluid," Proc. R. Soc. Lond. A **150**, 322–337 (1935).
16. O. T. Naman, M. R. New-Tolley, R. Lwin, A. Tuniz, A. H. Al-Janabi, I. Karatchevtseva, S. C. Fleming, B. T. Kuhlmey, and A. Argyros, "Indefinite media based on wire array metamaterials for the THz and mid-IR," Adv. Opt. Mater. **1**, 971–977 (2013).

Optics EXPRESS

17. A. Alchalaby, R. Lwin, A. H. Al-Janabi, P. W. Trimby, S. C. Fleming, B. T. Kuhlmey, and A. Argyros, "Investigation of plateau–Rayleigh instability in drawn metal–polymer composite fibers for metamaterials fabrication," J. Light. Technol. **34**, 2198–2205 (2015).
18. J. G. Hayashi, S. Fleming, B. T. Kuhlmey, and A. Argyros, "Metal selection for wire array metamaterials for infrared frequencies," Opt. Express **23**, 29867–29881 (2015).
19. M. G. Silveirinha, "Nonlocal homogenization model for a periodic array of ϵ-negative rods," Phys. Rev. E **73**, 046612 (2006).
20. H. K. Tyagi, H. W. Lee, P. Uebel, M. A. Schmidt, N. Joly, M. Scharrer, and P. S. J. Russell, "Plasmon resonances on gold nanowires directly drawn in a step-index fiber," Opt. Lett. **35**, 2573–2575 (2010).
21. J. G. Hayashi, "Wire array infrared metamaterial: Fibres fabrication and applications," Ph.D. thesis, University of Sydney, Australia (2017).
22. J. D. Love, W. M. Henry, W. J. Stewart, R. J. Black, S. Lacroix, and F. Gonthier, "Tapered single-mode fibres and devices. part 1: Adiabaticity criteria," IEE Proc. J, Optoelectron. **138**, 343–354 (1991).
23. R. J. Black, S. Lacroix, F. Gonthier, and J. D. Love, "Tapered single-mode fibres and devices. ii. experimental and theoretical quantification," IEE Proc. J, Optoelectron. **138**, 355–364 (1991).
24. S. Instruments, "Pipette cookbook 2015 - P-97 and P-1000 Micropipette pullers - Rev. E," https://www.sutter.com/PDFs/pipette_cookbook.pdf.
25. O. Photonics, "Spiricon Pyroelectric camera - Pyrocam IV datasheet," https://www.ophiropt.com/laser--measurement/beam-profilers/services/manuals.
26. E. Abbe, "Beiträge zur theorie des mikroskops und der mikroskopischen wahrnehmung," Arch. für mikroskopische Anat. **9**, 413–418 (1873).
27. S. Weisenburger and V. Sandoghdar, "Light microscopy: an ongoing contemporary revolution," Contemp. Phys. **56**, 123–143 (2015).
28. A. Tuniz and B. T. Kuhlmey, "Two-dimensional imaging in hyperbolic media–the role of field components and ordinary waves," Sci. Rep. **5**, 17690 (2015).
29. M. S. Habib, A. Tuniz, K. J. Kaltenecker, Q. Chateiller, I. Perrin, S. Atakaramians, S. C. Fleming, A. Argyros, and B. T. Kuhlmey, "Removing image artefacts in wire array metamaterials," Opt. Express **24**, 17989–18002 (2016).